Biomineralized Anisotropic Gold Microplate−Macrophage Interactions Reveal Frustrated Phagocytosis-like Phenomenon: A Novel Paclitaxel Drug Delivery Vehicle

Ajay Vikram Singh,[*,#,†] Madu Batuwangala,[#,‡] Ruchir Mundra,[§] Krunal Mehta,[§] Sanket Patke,[§] Ermelinda Falletta,[∥] Rajendra Patil,[⊥] and W. N. Gade[*,⊥]

[†]Department of Biomedical Engineering, Center for Biotechnology and Interdisciplinary Studies, Rensselaer Polytechnic Institute, Troy, New York 12180, United States

[‡]Freelance Writer and Editor, 4 Glemham Drive, Ipswich, Suffolk IP4 5BH, United Kingdom

[§]Department of Chemical and Biological Engineering, Center for Biotechnology and Interdisciplinary Studies, and Rensselaer Nanotechnology Center, Rensselaer Polytechnic Institute, Troy, New York 12180, United States

[∥]Dipartimento di Chimica Inorganica, Metallorganica e Analitica, Universita di Milano, Via G Venezian 21, Milano 20133, Italy

[⊥]Department of Biotechnology, University of Pune, Pune 411007, India

S *Supporting Information*

ABSTRACT: This study reports a facile biomineralization route for gold microplates (GMPs) synthesis using bovine serum albumin (BSA) as a reductant and stabilizing agent. Adding BSA to $HAuCl_4$ solution yields spontaneous versatile anisotropic and partially hollow GMPs upon aging. We hypothesize that the instantaneous protein denaturation at low pH enabled access to serine and threonine hydroxyl, and sulfhydryl groups of BSA, which act as a reductant and stabilizer, respectively. This reaction could be hastened by increasing the temperature well beyond 65 °C. Transmission electron microscopy/X-ray diffraction studies revealed highly crystalline and anisotropic structures (triangle, pentagon, and rectangle). Atomic force microscopy/scanning electron microscopy analyses demonstrated unique morphology of microplates with a partially void core and BSA mineralized edge structure. RAW 264.7 mice peritoneal macrophage−microplate interaction studies using live cell confocal imaging reveal that cells are capable of selectively internalizing smaller GMPs. Large GMPs are preferentially picked with sharp vertices but cannot be internalized and exhibit frustrated phagocytosis-like phenomenon. We explored particle phagocytosis as an actin mediated process that recruits phagosome-like acidic organelles, shown by a lysosensor probe technique. The biocompatible GMPs exhibited ∼70% paclitaxel (PCL) loading and sustained release of PCL, showing antitumor activity with the MCF-7 cell line, and could be a novel drug carrier for breast cancer therapy.

KEYWORDS: *biomineralizations, BSA, microplates, phagocytosis, paclitaxel*
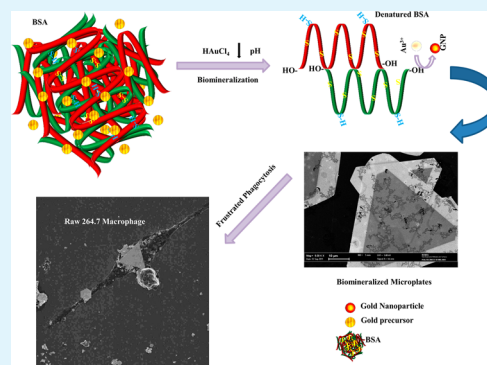
1. INTRODUCTION

The shape and size of nanoparticles and their physicochemical properties play a fundamental role in many important areas of research, such as biomedicine and biology.[1−3] These include particle targeting strategies in therapeutic applications, environmental fate of nanoparticles, and investigation of the rationale behind bacterial pathogen size and shape.[4] In addition to burgeoning interests in biocompatible nanoparticles based technologies, microscale anisotropic structures have recently had growing interest in medical and biological applications such as pharmaceutics, biosensors, and bioseparation technologies as well as affinity purification.[5,6] More recently, anisotropic 2D microstructures have gained importance because of their unique optical properties, potentially useful in chemical and biological sensing.[5] Due to the intense charge accumulation on the sharp corners and edges of the microplates, they are important substrates for surface-enhanced Raman scattering (SERS).[7]

Biological systems have intriguing capabilities to synthesize and assemble a range of inorganic ions into intricate biomineral anisotropic structures such as calcite, amorphous silica (diatoms), copper (*Escherichia coli*),[8] and magnetite (magneto-tactic bacteria).[9,10] The sophisticated natural biominerals are not only on a micro- to nanoscale but also few in number (e.g., Si/Ca), which often limits their technological expansion into biomedicine applications of biomineralized structures. Essentially, these limitations are due to a lack in diversity in the

availability of inorganic minerals, shapes, and synthesis routes.[9] In this context, protein is an excellent natural building block and has attracted much interest as a stabilizing agent to prepare microparticles due to its versatile functionality and excellent biocompatibility.[11] We have shown one pot, dual synthesis and stabilization of gold–silver nanoparticles, and their alloys in conjunction with platinum. Moreover, we utilized zwitterionic characteristics of BSA for binding, reducing, and alloying two inorganic metal precursors simultaneously.[12,13]

There are many biological routes for anisotropic metal nanostructure production using bottom-up nanoengineering.[14,15] However, there is a scarcity of reports depicting biocompatible synthesis recipes for microscale anisotropic structures. Recently, various techniques have been developed to synthesize microplates and their mechanism of formation has been elucidated using electron microscopy and theoretical modeling.[8,16] Protein microparticles have been reported but complex synthetic routes involving multistep protein activation spontaneous self-assembly (PASS) makes this approach cumbersome.[17] Though recently, gold microplates synthesis methods using serum albumin as a reductant and a stabilizer have been shown, but their anisotropic characteristics, especially the role of microscale geometry and size cutoff for biological applications, were not studied in depth.[18,19] Herein, we report a facile, room temperature (RT) recipe for anisotropic gold microparticle synthesis with diverse shapes, sizes, and physical structures. The atomic force microscopy (AFM)/transmission electron microscopy (TEM) and X-ray diffraction (XRD) studies displayed diverse anisotropic shapes and the highly crystalline nature of microplates synthesized. Scanning electron microscopy (SEM) coupled with AFM analysis demonstrated a unique morphology of the microplates with a void core and BSA mineralized, dense edge structure. RAW 264.7 cell–microplate interactions with macrophages revealed that smaller vertices can be selectively internalized over the larger ones. Actin transfection studies exhibited that actin mediated membrane wrapping is involved in "frustrated phagocytosis". Endocytosis demonstrates a lysosomal dependent mechanism is involved. As a proof-of-concept, paclitaxel loading and in vitro viability assay in breast cancer cell line GMPs exhibit a novel drug carrier. The results reported in this study can lead to promising applications of larger GMPs as drug delivery agents, based on geometrical and size advantages to evade phagocytosis.

2. MATERIALS AND METHODS

2.1. Anisotropic Microplate Preparation and Characterization.
A typical synthesis protocol includes addition of BSA (Sigma-Aldrich, A2058) in a 2–5 mg/mL range to 1 mM $HAuCl_4$ solution (Sigma-Aldrich, 254169), with gold salt solutions in excess (BSA:$HAuCl_4$ 3:1 or more as per mass/volume ratio). $HAuCl_4$ solution was prepared by dissolving a metallic Au sponge (purity 99.99%, Fluka) in aqua regia, diluted to the appropriate volume with water. The BSA–gold salt mixture was prepared in the appropriate buffer solution (phosphate buffered saline (PBS) or tris buffered saline (TBS)). Upon the addition of the gold salt, the color of the solution turns cloudy due to lowering of pH and protein denaturation, which turns into a clear solution after 2–3 h. As the reaction progresses, the shimmery appearance of the solution-containing vial indicates that reactions have been completed; the microparticles formed were accordingly characterized with TEM, XRD, SEM, and AFM. The entire synthesis was carried out at room temperature for 1 week or more. Alternatively, the reaction can be hastened to complete within 3–4 h via incubating samples in a dry oven at temperatures of 55–65 °C. The reaction product was collected by centrifugation at 10000 rpm

for 10 min. The Au microplates were washed three times with double distilled water to remove loosely bound BSA. The aqueous suspension of the Au product was drop-coated on a piece of silicon wafer (for AFM and SEM) or Formvar copper grid (for TEM) and dried under ambient conditions for characterization. SEM images were collected using a field-emission scanning microscope (JEM 840) operated at an accelerating voltage of 2 kV. TEM images were captured using a JEOL JEM 840 transmission electron microscope operated at 100 kV. An MFP 3D AFM instrument in multimode was used for height, amplitude, and phase imaging (Asylum Research). Images were collected in air under ambient laboratory conditions in tapping mode, using rigid silicon cantilevers mounting single crystal silicon tips (spring constant, 1.8 N/m; tip radius, <10 nm). For XRD studies, the approved International Centre for Diffraction Data sheet ICDD No. 4−0783 was utilized to resolve the diffraction pattern.

2.2. Macrophage and MCF-7 Cell Culture.
Continuous mice peritoneal macrophages (RAW 264.7) and human breast cancer cells (MCF-7), provided by American Type Culture Collection (ATCC), were used as the model cell lines for in vitro assays. The validity of results among macrophage populations of different species were verified by mouse peritoneal macrophage cells (J774). Cells were cultured in Dulbecco's modified Eagle's medium (DMEM, Gibco) supplemented with 10% heat-inactivated fetal bovine serum (FBS) and 1% penicillin/streptomycin (Sigma) in a cell incubator (37 °C, 5% CO_2, humidified). Macrophages were incubated on plain and IgG-coated coverslips to ensure that macrophages were capable of spreading and circular spreading of cells was confirmed using confocal microscopy (TCS-SP2 AOBS, Leica).

2.3. Time-Lapse Video Microscopy.
RAW 264.7 cells at seeding density of 5×10^4 cells/mL were allowed to attach in dishes lined with coverslip glass in DMEM media supplemented with 10% FBS and 25 mM 4-(2-hydroxyethyl)-1-piperazineethanesulfonic acid (HEPES, Sigma). The dishes were placed on TCS-SP2 AOBS (Leica) at 100× with proper phase contrast filters and equipped with the incubation chamber (H301-EC-BL, Okolab) to keep the cells at 37 °C. A microplate suspension containing mixed populations (0.5–15 μm) was added to the culture dishes at a ratio of one particle per cell, and bright-field phase contrast images were collected every 30 s for 2.5 h by a CoolSNAP HQ^2 CCD camera (Photometrics, AZ) connected to the METAMORPH software. Cells were observed for 12 h for long-term monitoring the phagocytosis processes and we observed the same cell behavior as for 2.5 h of culture. Observed cells were randomly chosen from the 4D files generated by the time-lapse acquisitions from the entire population. To avoid discounting potential bias due to macrophage size heterogeneity (radius 10 ± 2 μm), randomly selected images were processed, cropped, analyzed, and annotated using the LAS-AF Leica software.

2.4. Cell Transfection and Live Cell Lysosomal Tracking.
To investigate the role of actin in complete and or partial phagocytosis of GMPs, to analyze membrane ruffling of macrophages as well as study particle wrapping at the site of attachment and membrane retractions, we transfected RAW 264.7 with RFP expressing actin (Plasmid p^{CMV}LifeAct-TagRFP). Partial phagocytosis of larger microparticles was visualized by live imaging of actin transfected RAW 264.7 (LifeAct adenoviral kit, ibidi). Time-lapse images of phagocytosis were scored as one attached particle/single cell internalizations. Lysosomal activity was analyzed by incubating cells–microplates with LysoSensor Green DND-153 (Life Technologies) and time-lapse imaging.

2.5. Paclitaxel (PCL) Loading and Entrapment Efficiency into GMPs.
Paclitaxel (Santacruz Biotech) was dissolved in 100% ethanol to prepare a 1 mg/mL stock solution. A sterile solution was obtained by microfiltration. The drug loading efficiency was determined by mixing 1:1 (v/v) of paclitaxel and GMPs (1 mg/mL) in phosphate buffer saline (pH 7.4) at a final concentration of 25 μg/mL. The mixture was stirred overnight using a magnetic stirrer at 4 °C. The sample was centrifuged at 10000 rpm for 10 min. The supernatants after centrifugation were collected, and PCL content was quantified using a Jasco UV–vis spectrophotometer at 230 nm with a concentration/absorbance calibration curve at the same wavelength.[20]

The drug loading efficiency can be calculated from the following equation:

$$\text{PCL loading efficiency (\%)} = C_{PCL-GMPs}/C_{GMPs} \times 100\%$$

where, $C_{PCL-GMPs}$ = concentration of PCL in the GMPs and C_{GMPs} = concentration of GMPs

$$\text{PCL entrapment efficiency (\%)} = C_O - C/C_O \times 100\%$$

where, C = concentration of entrapped PCL (=concentration of PCL used in formulation − unbound PCL present in supernatant) and C_O = concentration of PCL used in formulation.

2.6. In Vitro Drug Release Studies. The PCL loaded GMPs, after centrifugation, were suspended in 5 mL of aqueous buffer solution at pH 7.4. The freshly prepared samples were placed into the dialysis membrane (molecular weight cutoff of 12−14 kDa, rinsed in acetone, and soaked for 24 h in the diffusion medium) of the diffusion chamber and were dialyzed in 100 mL of the diffusion media (freshly prepared saline phosphate buffer of pH 7.4, equilibrated at 37 °C). Aliquots of 1.0 mL of the diffusion medium were withdrawn at predetermined times from the sampling port and were replaced with an equal quantity of a fresh diffusion medium to maintain a constant volume. To analyze the released PCL in the diffusion media, PCL content was quantified using a Jasco UV−vis spectrophotometer at 230 nm with a concentration/absorbance calibration curve at the same wavelength. All measurements were performed in triplicate and the SD was calculated. To quantify the loading amount of a drug in terms of weight, thermal gravimetric analysis (TGA) was performed on an automatic thermal analyzer system TG/DTA (Diamond TG/DTA 8.0, PerkinElmer, USA). Test samples (3 mg) were placed in sample pans (platinum). The temperature was held for 30 min after the sample was heated under a constant argon flow at a rate of 5−10 °C/min to 100 °C to remove the residual solvent. Afterward, the temperature was raised to 700 °C at a rate of 50 °C/min to heat the samples.

2.7. Cell Viability Assay. Colorimetric MTT assay was used for cytotoxicity assay as described earlier.[21] In brief, γ-ray sterilized GMPs (with and without PCL) were incubated with different time points (1−7 days in vitro: DIV) and the toxic effect was evaluated using MTT assay kit (Sigma) as per manufacturer instructions. Cells were maintained with continuous exposure of GMPs or PCL loaded GMPs. After definite exposure, cells incubated with MTT solution and absorbance of colored formazan product was obtained at 570 nm in test samples and control cells (MCF-7 without treatment). Percent cell viability was determined by normalization of test samples absorbance divided by control.

2.8. Immunostaining and Scanning Electron Microscopy. Breast cancer cell line MCF-7 cells were seeded with PCL loaded microplates and incubated at 37 °C for 3 days in vitro. The cells were fixed with 4% paraformaldehyde (Sigma) for 30 min and washed with TBS, permeabilized with 0.5% Triton X-100 (Aldrich) for 10 min. The fixed cells were incubated in cytoskeletal buffer (10 mM MES, 138 mM KCl, 3 mM MgCl$_2$, 2 mM EGTA, and 0.32 M sucrose) for 30 min. For cytoskeleton (actin/tubulin) double staining, the cells were incubated with phalloidin−TRITC (1:400; Invitrogen) and anti-α-tubulin (1:200, sigma) for 1 h. After secondary antibodies staining, the samples were counterstained for nucleus (DAPI), fixed, and viewed at 40−63× magnification. For SEM, fixed cells were dehydrated as described in previous reports after 3 days of incubation with MCF-7.[22]

2.9. Statistical Analysis. All data are presented as mean ± SD unless specified otherwise. One-way ANOVA with a confidence interval of 95% and Student's t-test followed by posthoc analysis with Tukey's test were used to evaluate the statistical significance. The significance level was set at $p \leq 0.01$. Throughout this study, at least five independent experiments were performed in triplicate for statistical validation.

3. RESULT AND DISCUSSION

3.1. Gold Microplate Synthesis via Biomineralization of BSA: TEM and XRD Analysis. BSA protein has a unique globular structure, which is rich in serine (Ser or S, 32 units) and threonine (Thr or T, 35 units) amino acids.[23] These residues bear hydroxyl groups, which are reported as mild reducing agents able to produce nanoplates of numerous inorganic noble metals.[24] In this study, we report gold microplate synthesis of diverse shapes, via adding a gold salt precursor in a higher ratio to albumin. A low pH facilitates reduction reactions between HAuCl$_4$ and denatured BSA, spontaneously forming GMPs in 1 week. We hypothesize that anisotropic growth of the microplates upon aging with versatile shapes occurs primarily based on "nucleation and seed" mediated growth.[25] The microstructure development involves aggregation based crystal growth via attachment of AuCl$_4^-$ ions (seed) to the denatured BSA organic template (nucleation site). A biomineralized albumin−gold hybrid structure evolves by eliminating water molecules at microplate interfaces, forming ionic and van der Waals bonds via a range of physiochemical interactions.[26] First, adding equimolar HAuCl$_4$ to BSA solution with gold salt in excess (3:1 or higher) at room temperature (RT) brings down the pH of the solution from 7.4 to 3, and the solution becomes partially cloudy (Figure S1B−E, Supporting Information). This indicates that an acidic condition promotes denaturation and unfolding of BSA, opening hydroxyl cryptic sites in Ser and Thr residues, which mildly reduce Au^{3+} → Au^{1+} (turning the solution from yellow to cloudy). However, the population of reduced gold to nanoparticles (Au^0) remains below the detectable SPR threshold.[12] When this solution is left at room temperature, progressive denaturation of protein and successive reduction of gold ion reaches a critical concentration where the available salt precursor concentration exceeds that of albumin molecules. At this stage, the available sulfhydryl groups, which apparently act as the protein capping and stabilizing agents, promote interactions of AuCl$_4^-$ ions with different crystallographic facets of the initially formed nuclei. In solution, reductant hydroxyl ions in BSA become exceedingly low upon aging. This avails more salt precursor per nuclei, thereby allowing the growth of microplates (Figure 1). Further, the biomineralized shell of BSA−gold crumbles, forming versatile microplates such as hexagons, trapeziums, triangles, and prisms.
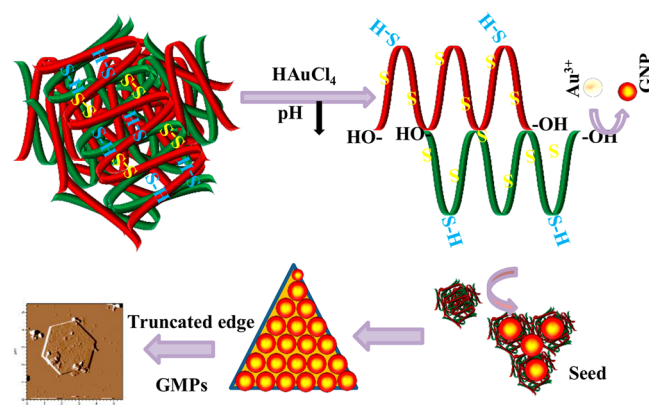

Figure 1. Schematic of anisotropic microplate synthesis. Adding gold salt solution lowers pH and denatures proteins. Unfolding BSA exposes reductant hydroxyl groups in threonine and serine, and the sulfhydryl group stabilizes GMPs. Both −OH and −SH groups are instrumental to the synthesis of Au microplates of different shapes because a sulfhydryl group can provide an additional reactive site for attaching the BSA molecule to the Au surface and thus stabilizing the final product. The inset shows AFM images of anisotropic structures.

14681

dx.doi.org/10.1021/am504051b | ACS Appl. Mater. Interfaces 2014, 6, 14679−14689

BSA molecules are expected to preferentially adsorb on the [111] facets during anisotropic microplate growth, apparently suppressing the growth along the [111] direction after saturation; hence growth shifts along the [100] anisotropic direction, yielding various anisotropic microshapes.[27] The kinetics of the delayed reduction could be manipulated and accelerated through temperature variations. Au^{3+} reduction could be hastened to complete the reaction with high yield of microplates (~90%) within couple of hours via raising the temperature of samples to 60−70 °C for 2−3 h.[19] The growth of giant microstructures explained here is of particular interest because it occurs spontaneously at room temperature when denatured BSA−gold salt solution is left unattained for weeks, mimicking biomineralization processes in nature.[21,28] In addition, it provides a convenient explanation and opportunity using certain types of defects in solids for the growth of anisotropic structures as an advanced materials synthesis recipe.

The formation of the BSA mineralized gold microplate can be confirmed by the combination of optical, transmission electron microscopy (TEM), and selected area electron diffraction (SAED) pattern analysis. The UV−vis-NIR absorption spectra of gold microplates displayed broad peaks in the visible and near-infrared regions (Figure S1, Supporting Information). A single population of anisotropic structures such as prisms is formed under sustained slow kinetics of a spherical nanoparticles assembly and exhibits a shift of spectra from UV−vis to NIR.[29] The complex shape of UV−vis-NIR spectra appearing in our study might be due to the multifaceted anisotropic structure viz. prism trapezium to a diverse population of hexagons.[29] The TEM and SAED patterns of BSA mineralized $AuCl_4$ after 2 weeks aging show a large number of anisotropic microstructures (Figure S2A−E, Supporting Information). The solution appears clear and shimmery yellow due to the presence of large microplate populations. The majority of the microshapes observed were triangles and prisms, followed by hexagons with quite a few quasi-spherical GMPs, after the AFM/SEM morphology analysis (Table 1). The SAED patterns of the gold micro-

Table 1. Quantification of Morphological Parameters of Anisotropic Microplate Population

anisotropic microplates	mean edge (longest) (μm)	mean edge (shortest) (μm)	mean thickness (nm)	yield (%)
regular hexagon	15 ± 1.5	5 ± 0.5	150	<8
irregular hexagon	15 ± 1.5	2 ± 0.5	450	~12
trapezium	17.5 ± 0.5	5 ± 0.5	150	10
triangle	17.5 ± 1	5 ± 0.5	200	52
quadrilateral	17.5 ± 2.0	5 ± 0.5	200	13
truncated rod/ cylinders	20 ± 3	NA	100	<5
quasi spherical	Ø = 2.5 ± 0.5	NA	NA	<5

triangle (Figure S2B inset, Supporting Information) were taken by directing the electron beam perpendicular to the flat faces. The hexagonal symmetry of the diffracted spot exhibits the single crystalline nature of the synthesized microstructures. The three sets of SAED patterns can be indexed to the square 2/3[422], triangle [220], and circle 1/3[422] Bragg reflections appearing from the fcc gold structure.[30] The Braggs diffraction 1/3[422], which are forbidden reflections, give clear evidence

of stacking faults in the [111] plane, perpendicular to the electron beam. This disrupts the fcc symmetry of gold and yields anisotropic, plate-like microstructures. The kinetics of slow reductions, derived from the mild reduction potential of BSA, could be the plausible cause of planar defects and the origin of anisotropy. Bragg's reflections obtained correspond to the fcc crystalline structure of the gold microtriangles (Figure S2F, inset, Supporting Information). The most intense peaks appearing at 2θ = 38.2° correspond to Bragg reflection for the [111] oriented, flat gold microtriangles on the planar surface.[31] The minuscule peak [220] and [311], with lattice spacing of 1.44, originates from the triangular morphology of the diffracted spot. Notable, observation of the low intensity peak ratio of [200] and [111] diffraction is an important rational of increasing dimension of the synthesized microplates.[32]

3.2. Microscopic (AFM/SEM) Characterization Manifest Microplate's Partial Hollow Three-Dimensional Core. The mean edge/facet length and morphological details were numerically calculated and compared with the anisotropic symmetries observed in SEM and AFM for validations (Table 1, Figure S2G,H, Supporting Information). To investigate the surface topography of synthesized polyhedron microplates, AFM investigation was carried out in contact mode. The height and amplitude images give an estimate to both lateral (xy) and height (z) measurements of a representative hexagon microplate (Figure 2A,B). The microprism and plates observed under contact mode were seemingly flat with mostly sharp angles and vertices. For each morphological map of microplates, a phase or friction map has been acquired to study topography (Figure 2C). Phase signal from two different materials surfaces (e.g., metallic gold versus organic BSA) can be resolved via AFM tip interaction, depending on the mechanical, chemical, and structural properties of the surface.[22] For images acquired in contact mode, the friction signal has a similar role to the phase in tapping mode because it depends on mechanical and chemical properties of the surface and reveals finer detail between different nanobiosurfaces.[22] However, we did not observe a qualitative difference in phase map of GMPs, which might be due to the mixed (heterogeneous) nature of the biomineralized plate, which makes it difficult to make a contrast due to variation in the BSA and mineralized gold phase.

SEM, another complementary technique for high-resolution surface investigations, enabled us to clearly view the partial hollow core and sharp facets in GMPs (Figures 2E−L and S2I−K, Supporting Information). Many small microstructures can be seen attached over giant polyhedron of different microshapes (red arrowhead). Particularly, a truncated rectangular tube-like or rod shaped microstructure is shown in Figure 2E,G, respectively. The SEM large field depth has the ability to image the undercuts of high aspect ratio structures at different cross sections.[33] A high resolution, backscattered SEM image of biomineralized microplates is shown in Figure 2K,L; the magnified box indicates the contrast based on the differences in atomic components of BSA and gold, and demonstrates heterogeneous surface compositions. The brighter areas with granular morphology could be albumin-mineralized gold nanoclusters, as described "seeds" for anisotropic growth of the microstructures because protein mediated biomineralization produces hybrid bioinorganic microstructures over aging.[34] Sequential magnification reveals the sharp edges and undercuts present in partially hollow internal spaces of discrete shapes. It is more evident in the magnified images of Figure 2I,J (box) where under cut on one side of facet and slope on the others
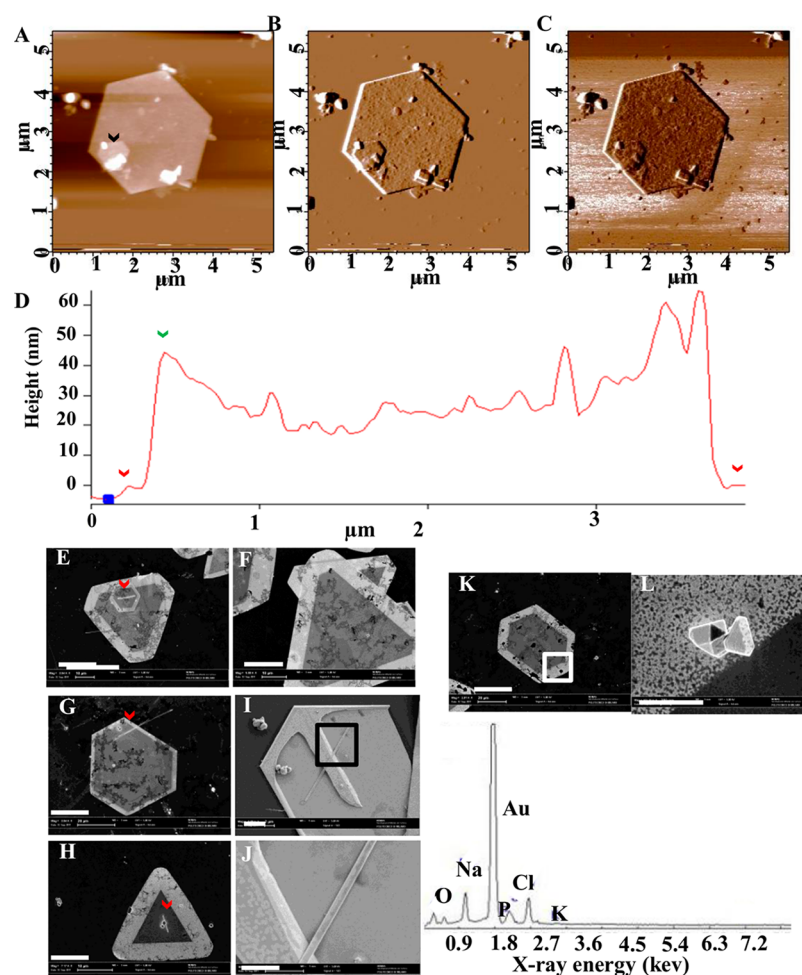
Figure 2. AFM and SEM characterization of microplate topography and surface profile. (A−C) Top views of topographic, amplitude, and phase maps of the hexagon microplate. Black arrowhead demonstrates small anisotropic structures adhered to large microplate. (D) Line scans of hexagon showing height and length profile (red and green arrows: outer and inner edges, respectively). (E−K) SEM images showing morphology and surface profile of different microplate shape. Red arrow show tiny microstructures present over larger microplates. (I,J) Micrograph with undercuts and partial hollow internal volumes, which is clearer in three-dimensional views of magnified box regions. (K,L) Magnified edge (box) demonstrates biomineralized edges with granular BSA−gold clusters and elemental analysis of biomineralized BSA microplate (scale bar: E−H 10 μm; K 20 μm; I 2 μm; J,L 0.5 μm).

are clearly visible. The SEM sample stage slope can be tilted at different angles during imaging, which results in an increase in electron emission from the sample surface. It produces higher resolution and intensity in z-direction, thereby making undercuts visible. X-ray signals from samples are commonly used to provide elemental analysis via energy-dispersive spectrometry (EDS) attached with SEM. The panel below panels K and L of Figure 2 shows the elemental compositions of backscattered SEM image of biomineralized GMPs where the prominent gold peak is clearly visible.

3.3. Macrophage−GMPs Interactions Exhibit Membrane Wrapping and Frustrated Phagocytosis-like Phenomenon with Large Microplates. An in vivo surveillance system utilizes a slower method of foreign body clearance using specialist immune cells called macrophages, which are mobile and patrol continuously in the systemic circulation system. They ingest everything that is detected as foreign to the body, clearing via a process called phagocytosis. However, when the aspect ratio and diameter of a foreign object extends beyond 5−10 μm, it leads to an interesting situation. Macrophages, being unable to fully enclose it, struggle

to clear a foreign object, leading to a stressful situation for the cell called "frustrated phagocytosis".[35]

Phagocytosis has been shown to have major obstacles in drug delivery in vivo because macrophages rapidly internalize drug delivery carriers with their therapeutic payload and invoke rapid clearance from systemic circulation. Therefore, to propose applicability of GMPs for drug delivery with a partially hollow core, with on par dimensions for phagocytosis, we followed live imaging of GMPs−macrophage interactions. The objective of the study was to probe if inorganic microplate size and shape can be utilized to inhibit phagocytosis, which could be used as drug carriers in vivo.[36] We tested anisotropic microplates with different geometries (e.g., hexagon, triangles) by incubating with the macrophages, and observed under a light microscope (100×) with time-lapse video microscopy (Figures S3 and S4 and Movies S1−S4, Supporting Information). Like previous studies with opsonized polystyrene (PS) particles of diverse geometries with a relatively average aspect ratio of 6 μm, we also observed that almost all polyhedron shapes were capable of initiating phagocytosis in at least one orientation.[36,37] But only a few shapes with a low aspect ratio (≤3 μm) were phagocytosed completely. As shown with an arrow, a triangle
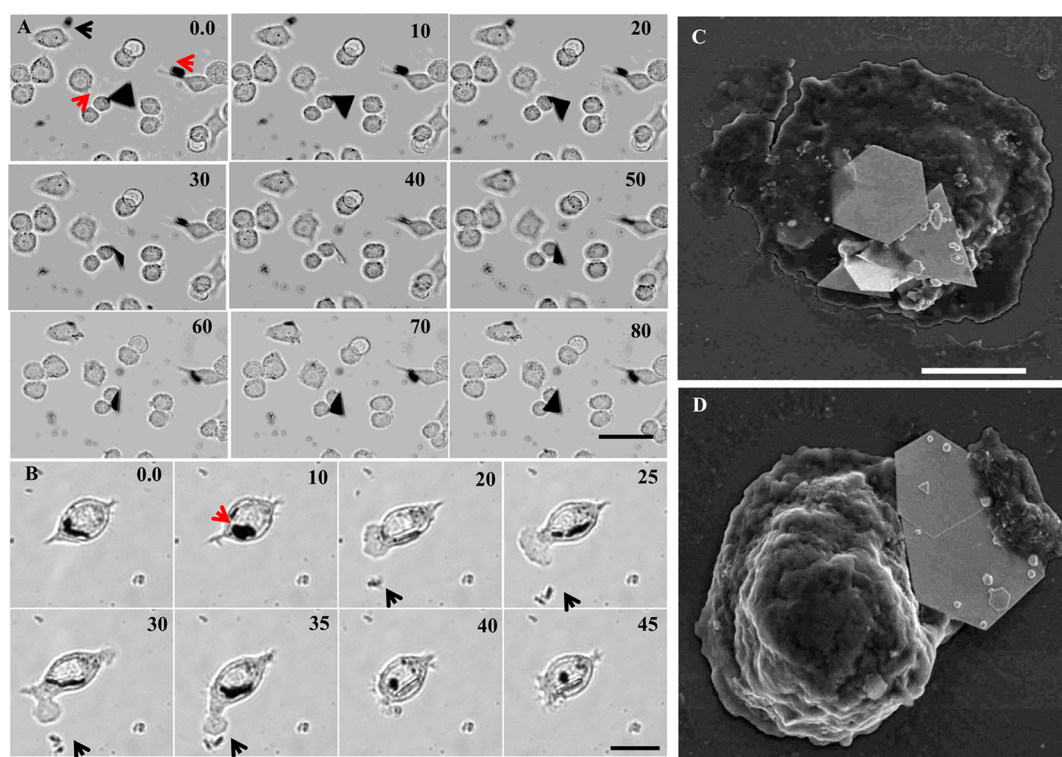
Figure 3. Microscopic analysis of macrophage−GMP interactions. (A) Snapshot of time-lapse videos showing a small microplates (black arrowhead, edge length <3 µM) in the process of being phagocytized (0−30 min) and internalized after 40 min. Large triangles and hexagons (red arrowhead) with an average edge length >3 µm. Macrophages show the frustrated phagocytosis-like phenomenon with partial phagocytosis. A cell interacts with the triangle microplates through the vertices and the resultant membrane pulling positions plate in different orientations but it is not internalized, even after 1.5 h. (B) Snapshots show RAW 264.7 extending membrane protrusions to catch and internalize a cluster of small GMPs (black arrows), whereas large a GMP could be seen constantly attached with cell interior but never fully phagocytosed. (C,D) SEM micrograph of cells holding microplates with membrane cup. (D) Partially phagocytosed hexagon and triangle (scale bar: A,B 10 µm; C,D 5 µm).
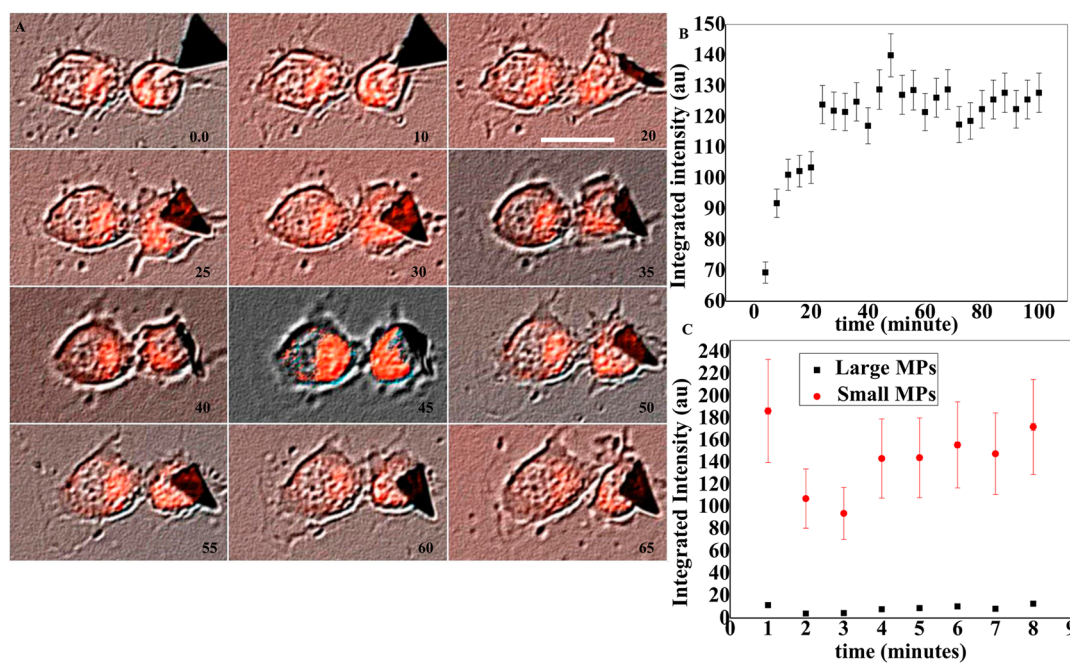

Figure 4. Transfected RAW 264.7 shows actin dependent phagocytosis. (A) Overlay of phase contrast and fluorescent clips from time-lapse videos showing RFP expressing actin wraps around larger triangular microplates during process of partial phagocytosis as seen by fluorescent region over microtriangle at different time points. (B) Quantification of integrated fluorescent intensity of RFP actin over microtriangle as region of interest (ROI) corroborates that RFP tagged actin mediated wrapping of microtriangle is responsible for holding and rotating in different orientations, while unable to engulf it completely (scale bar: 15 µm). (C) Quantified lysosensor activity shows significant difference in involvement of phagosome-like acidic compartment in larger vs smaller GMPs phagocytic process.
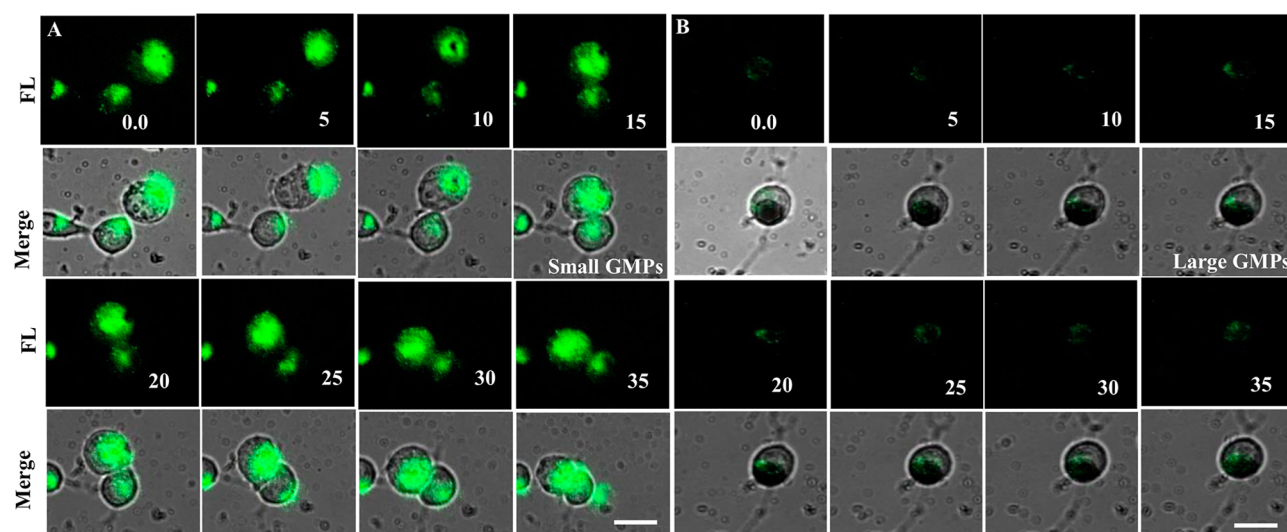
Figure 5. LysoSensor Green DND-153 staining phagosome-like activity. (A) Live cell tracking of macrophages demonstrating acidic phagosome-like activity in cells phagocytizing smaller GMPs as stained by green lysosensor probe. (B) Larger particle shows lesser phagosome-like activity (scale bar: E,F 50 μm).

and quasi-spherical particle are completely internalized after 1 h of incubation with RAW 264.7 in culture (time-lapse clips in Figure 3A, Movie S1, Supporting Information). Intriguingly, large anisotropic microplates were preferentially grabbed through a pointed edge with sharp vertices by macrophages. As shown in time-lapse images of Figure 3A (Figure S3 and Movie S2, Supporting Information), RAW 264.7 pulled and pushed a large microtriangle at different orientations but still could not internalize. An interesting aspect of large GMPs—macrophage interactions is that a macrophage latches onto an acute angled tip or snipped edge of GMPs with large dimensions (>3 μm), irrespective to their aspect ratio and geometry. This is probably due to easy piercing of sharp tips into the membrane upon initial contact. Then, they spread along the diverging facets but are unable to internalize fully due to presence of diverging edges and complex facets, converse to previous reports studied with smooth surfaces.[36] Cell protrusion and membrane extension of macrophages in the process of phagocytosis can be clearly seen in snapshot images of Figure 3B. The movie clip shows a wandering RAW 264.7 observes a small microplate and starts membrane extensions toward GMPs (red arrowhead) and wraps and internalizes particles (Movie S3, Supporting Information). SEM imaging provided more evidence of partial internalization and membrane wrapping around larger GMPs. Partially embedded GMPs (Figure 3C) and a macrophage membrane extension holding a large hexagon with a cup shape membrane structures is demonstrated in Figure 3D. Many cells exhibit active interactions with diverse microshape (e.g., microhexagon, microtriangles) simultaneously but after 2−3 h, leave the larger GMPs (Movie S4, Supporting Information).

3.4. Microparticle Phagocytosis Is an Actin Mediated Process. Regardless of target geometry and shape, most phagocytic mechanisms follow remodeling and arrangement of actin cytoskeleton.[38] In many endocytic pathways including large particles uptake, such as macropinocytosis, actively involve "actin cup" formation and membrane wrapping as phagosomes surround microparticles.[39] Next, we investigated the role of actin in the partial phagocytosis of GMPs. As shown in snapshots of time lapse videos, phase and fluorescence overlay

of actin transfected macrophage interacts with a large microtriangle (Figure 4A), conforming that the current mechanism involves active gripping of GMPs with variable actin phagocytic cups. As evidence, the scatter plot of the z-axis profile, drawn from different stacks of florescent imaging (Figure 4B), shows steady variation in the mean intensity of RFP tagged actin. This demonstrates that cell and large GMPs interaction indeed involve repeated events of actin mediated membrane gripping and actin ruffling during the pull−push of GMPs.

The failure of large GMPs internalization reported in this study could be correlated with the complex interplay of the thermodynamic force of the cell membrane wrapping and the delayed receptor diffusions kinetics due to multifaceted microplate−cell membrane interactions. Combined interplay of disturbed kinetics of receptors−ligand interaction at the binding site and free energy required to drive the GMPs into the cell could be the vital factors governing the frustrated phagocytosis.[40] Another interesting aspect of these partially hollow metal microplates is that due to their larger dimensions, they could promote higher ligand−receptor interaction. Therefore, unlike smaller particles, which undergo endocytosis at a faster rate in systemic circulation due to limited membrane interactions, GMPs could be used as novel drug carriers without phagocytosis. Moreover, anisotropy in itself is a hindrance to endocytosis of GMPs, adding more value for the microplates reported here as a drug delivery vehicle.[41] Also, cetrimonium bromide (CTAB), as a stabilizing agent for the synthesis of anisotropic structures reported in previous studies, acts as an obstacle for protein functionalization for targeting, which limits their uptake.[40]

3.5. Macrophages Recruit Phagosome-like Acidic Organelles for GMPs Internalization. The phagocytic pathway of mammalian cells comprises actin based distinct membrane compartments, which internalize, degrade, or recycle them, and often involve low pH compartments such as endosomes and lysosomes.[42] To determine whether a lysosome is involved in actin mediated internalization during the early steps in frustrated phagocytosis shown here, we further performed live cell imaging of RAW 264.7−GMPs
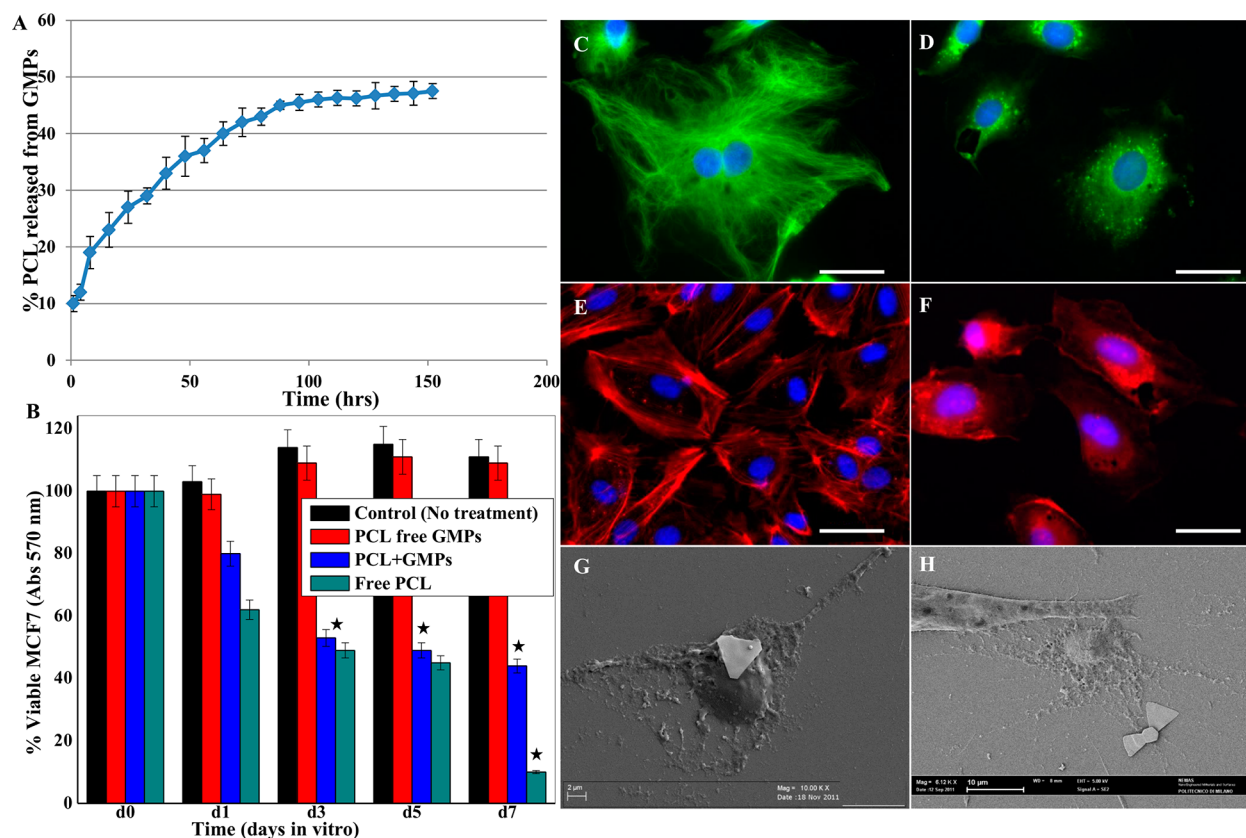
Figure 6. Assessing paclitaxel release from GMPs, in vitro cytotoxicity and influence on cell cytoskeleton and morphological changes. (A) In vitro drug release for microplates. (B) MTT test results showing time dependent cell viability in MCF-7 cells. All data points presented as mean ± SD obtained from five independent experiments implemented in triplicate. (C,D) Densely packed cytoplasmic microtubulin network (anti-β tubulin FITC: green) emanating from microtubule organizing center (MTOC) in proximity of the nucleus (DAPI: blue) is seen in control cells (6C). Contrary, PCL−GMP treated MCF-7 cells exhibit unorganized and decentralized fibers with diffused signals (6D). Scale bar: 10 μm. (E,F) Similarly, control cultures demonstrate well organized α-actin fibers pursing nucleus, primarily orientated along cellular axis whereas PCL treatment causes loss in circumferential disorientation and α-actin debundling to organize as microcables. (G,H) SEM micrograph showing internal structures of MCF-7, which partially engulfed PCL loaded microplates, reveal disintegrated membranes and morphology integrity.

interactions in the presence of lysosensor probes. The weakly basic amine probes selectively accumulate and fluorescently label the internal cellular compartments with acidic pH, which is crucial to investigate the biosynthesis of lysosome around phagocytic structures surrounding GMPs.[43] Probes have high selectivity for acidic organelles and freely permeate to cell membranes, and could be vital to understand endocytosis and intracellular transport of anisotropic microstructures.[39] Lysosensor probes evidently demonstrate that smaller particles (<3 μm) distinctly involve lysosomal activity, as we quantified significant differences in fluorescent intensity (Student's t-test; p-value ≤ 0.0001) between small vs large GMP phagocytosis (Figure 5A−C). As shown in phase contrast and immunofluorescence overlay images, initial snapshots of RAW 264.7 phagocytosis of smaller microplate interactions exhibit qualitatively higher fluorescence compared with larger particles with partial phagocytosis (Figure 5A,B). The left panel demonstrates higher and dynamic variations in lysotracker probe activity with a small particle and the right panel shows RAW 264.7 with a large hexagon trapped over the cell with minimal or no fluorescence. Therefore, live cell tracking with lysosensor probes demonstrates that cells recruit a phagosome-like acidic compartment during microplate phagocytosis.

3.6. Evaluating GMPs as Novel Drug Carrier: Paclitaxel Loading and in Vitro Cytotoxicity. Albumin-bound

paclitaxel has been shown to enhance the antitumor activity of the drug via selective binding of a drug−BSA conjugate over the albumin receptor gp60, which is overexpressed in endothelial cells surrounding a tumor.[44] This encouraged us to test the albumin biomineralized microplates as a paclitaxel drug carrier supported by the shape and size induced frustrated phagocytosis observed with the RAW 264.7−GMP interaction. In an attempt to predict the in vivo behavior of the BSA mineralized GMPs, we incubated microparticles with paclitaxel and studied drug entrapment and loading efficiency. We observed ∼70% PCL entrapment (or ∼60% by weight as determined by TGA) in particle hollow core and biomineralized shell of GMPs. We hypothesize that the porous BSA mineralized anisotropic shell, as shown in Figure 2L SEM images, and internal partially void spaces of GMPs synergistically enhance trapping and loading efficiency of PCL, making microplates a promising drug carrier. We analyzed the mean surface area of GMPs more than 90 m^2/g, which putatively may enhance drug loading efficacy of biomineralized GMPs. As shown in Figure 6A, in vitro drug release demonstrates approximately 37% PCL release during the initial 48−60 h, which slightly increases to 44% during the next 24 h. After day 4 onward, a slower and continuous, approximately first-order release is observed.

After the in vitro drug release study, we incubated PCL–GMP conjugates with breast cancer cell line MCF-7 cells and quantified in vitro cell viability using MTT assay. PCL free GMPs and PCL without GMPs were used as a control. We treated MCF-7 with the same concentration of PCL free GMPs, which were used for drug loading assays. Unlike previous studies, which emphasize both time and concentration dependent in vitro antitumor activity, we emphasized only time dependent toxicity evaluation using only one concentration, 25 μg/mL, for studies, which has been reported as an optimal toxic concentration in many in vitro assays.[45] As shown in Figure 6B, after 24 h of incubation, PCL loaded microplates show less toxicity than free PCL, which is obvious as the in vitro drug release during the initial 24 h is less than 20%; however, after 1 day and onward, GMPs with and without PCL show time dependent cytotoxicity that is significantly higher compared with the control and PCL free GMPs. Contrary, GMPs in the absence of drug show high biocompatibility throughout incubation as viability is close to that of the control. After day 7, the free PCL sample shows a significant drop in cell viability whereas GMPs with PCL show comparable viability in days 5−7. It could arise due to slight adoption to the surrounding environment by MCF-7 cells, exposed to sustained drug release from the PCL loaded microplates. We obtained a good loading efficiency and controlled release of the PCL from the GMPs, which could be due to several reasons. First, unlike previous PCL loading with polymeric NPs, which involve interfacial deposition or nanoprecipitation, in our study, the internal hollow core of the microplate could physically trap and steadily release PCL molecules over time.[46] Second, at the bio-nano interface, interactions between PCL and pore network of mineralized BSA may alleviate molecular diffusion of a drug along the pores.[47] Lastly, corona properties of mineralized gold−BSA at the GMPs core−shell interface may synergistically influence PCL payloads and passive release rates of a drug.[48]

Next, we looked morphological and cytoskeleton changes in MCF-7 cells induced by PCL loaded in microplates using confocal and scanning electron microscopy. As show in Figure 6C−F, actin and microtubulin organization is well preserved with radiating tubulin fibers and straight actin filaments in the control MCF-7 cells. Contrary, PCL release from microplates caused cytoskeleton disarrangement, which results in changes in cell size and shape, which are in agreement with previous reports showing the effect of PCL in an in vitro model.[49] Morphological stability, MCF-7 membrane integrity, and influence of PCL on changes in cell surface structures were assessed with SEM. Cells were incubated with PCL−GMPs conjugate for 3 days and then fixed and imaged with SEM. Figure 6G,H shows two adjacent MCF-7 cells; the cell that embed GMPs with PCL has a completely loose cell architecture whereas the neighboring cell without the GMP conjugated drug is relatively healthy. It proves that a partially hollow microplates core slowly releases PCL, which over time, completely disintegrates the cell cytoskeleton, in corroboration with immunofluorescence analysis shown above. Further experimental studies of PCL loaded microplates in animal models are essential to precisely appraise the risks and benefits of local delivery of PCL in a tumor using microplates reported here.

4. CONCLUSION

We described here a facile room temperature synthesis protocol of anisotropic microplates of diverse shape and size. GMP−macrophage interactions demonstrated the frustrated phag-ocytosis-like phenomenon with RAW 264.7. Paclitaxel loading displayed good drug entrapment efficiency, sustained release of the drug, and reduction in cell viability of breast cancer cell line MCF-7, comparable with free paclitaxel. As a proof-of-concept study, the protocol described here demonstrates the feasibility of biocompatible BSA−gold microplate production with internal volume, which puts forth an interesting perspective as drug delivery carriers. However, unlike previous reports of geometrically controlled synthesis of an array of IgG-opsonized anisotropic polystyrene microparticles,[36,50] we produce a mixed population of biomineralized gold microplates. The standardization of protocol for calibrated GMP production will open many new perspectives for scaling up and extending this technology for cancer hyperthermia and drug delivery vehicles. Another limitation, considering its polyhedron shape with sharp tips and micrometer size, is its probability to block the smaller blood vessels when used for systemic delivery. Recent simulation studies demonstrated that the anisotropic particles align perpendicular to the fluid flow direction, blocking narrow microchannels.[51] This limits microplate technology for localized surface applications as therapeutic agents.

■ ASSOCIATED CONTENT

Ⓢ Supporting Information

UV−vis−NIR absorption spectra of gold microplates, images of gold salt solution before and after adding BSA and after 5 h and 1 week, TEM and XRD analysis, montage of stack image showing RAW 264.7 and large microtriangle interaction, montage of time-lapse phase contrast image showing macrophage interactions with a large microhexagon, triangle and GMPs cluster, thermogravimetric analysis of drug loading in terms of weight, time-lapse video of sparsely seeded RAW 264.7 cell line incubated with microplates, time-lapse video of sparsely seeded RAW 264.7 cell line incubated with microplates, time-lapse video of single RAW 264.7 cell incubated with diverse microplates populations and time-lapse video of single RAW 264.7 cell line incubated with microplates mixed populations. This material is available free of charge via the Internet at http://pubs.acs.org.

■ AUTHOR INFORMATION

Corresponding Authors
*Ajay Vikram Singh. E-mail: singha8@rpi.edu. Tel: +1-518-276-2065. Fax: 518-276-4233.
*W. N. Gade. E-mail: wngade@unipune.ernet.in.

Author Contributions
[#]These authors contributed equally. The paper was written through contributions of all authors. All authors have given approval to the final version of the paper.

Notes
The authors declare no competing financial interest.

■ ACKNOWLEDGMENTS

■ REFERENCES

(1) Nolan, J. P.; Mandy, F. Multiplexed and Microparticle-based Analyses: Quantitative Tools for the Large-Scale Analysis of Biological Systems. *Cytometry, Part A* **2006**, *69A* (5), 318−325.

(2) Balmert, S. C.; Little, S. R. Biomimetic Delivery with Micro- and Nanoparticles. *Adv. Mater.* **2012**, 24 (28), 3757−3778.

(3) An, K.; Hyeon, T. Synthesis and Biomedical Applications of Hollow Nanostructures. *Nano Today* **2009**, 4 (4), 359−373.

(4) Hassan, S.; Singh, A. V; A, V. Biophysicochemical Perspective of Nanoparticle Compatibility: A Critically Ignored Parameter in Nanomedicine. *J. Nanosci. Nanotechnol.* **2014**, 14 (1), 402−414.

(5) Sajanlal, P. R.; Sreeprasad, T. S.; Samal, A. K.; Pradeep, T. Anisotropic Nanomaterials: Structure, Growth, Assembly, and Functions. *Nano Rev.* **2011**, 2, 5883_1−5883_62.

(6) Fischer, T.; Agarwal, A.; Hess, H. A Smart Dust Biosensor Powered by Kinesin Motors. *Nat. Nanotechnol.* **2009**, 4 (3), 162−166.

(7) Xiong, Y.; McLellan, J. M.; Chen, J.; Yin, Y.; Li, Z.-Y.; Xia, Y. Kinetically Controlled Synthesis of Triangular and Hexagonal Nanoplates of Palladium and Their SPR/SERS Properties. *J. Am. Chem. Soc.* **2005**, 127 (48), 17118−17127.

(8) Xia, Y.; Xiong, Y.; Lim, B.; Skrabalak, S. E. Shape-Controlled Synthesis of Metal Nanocrystals: Simple Chemistry Meets Complex Physics? *Angew. Chem., Int. Ed.* **2009**, 48 (1), 60−103.

(9) Bansal, V.; Bharde, A.; Ramanathan, R.; Bhargava, S. K. Inorganic Materials Using "Unusual" Microorganisms. *Adv. Colloid Interface Sci.* **2012**, 179−182, 150−168.

(10) Singh, A. V.; Patil, R.; Anand, A.; Milani, P.; Gade, W. Biological Synthesis of Copper Oxide Nano Particles Using Escherichia coli. *Curr. Nanosci.* **2010**, 6 (4), 365−369.

(11) Tan, C. J.; Chua, H. G.; Ker, K. H.; Tong, Y. W. Preparation of Bovine Serum Albumin Surface-Imprinted Submicrometer Particles with Magnetic Susceptibility through Core−Shell Miniemulsion Polymerization. *Anal. Chem.* **2008**, 80 (3), 683−692.

(12) Singh, A. V.; Bandgar, B. M.; Kasture, M.; Prasad, B. L. V.; Sastry, M. Synthesis of Gold, Silver and Their Alloy Nanoparticles Using Bovine Serum Albumin as Foaming and Stabilizing Agent. *J. Mater. Chem.* **2005**, 15 (48), 5115−5121.

(13) Singh, A. V.; Patil, R.; Kasture, M. B.; Gade, W. N.; Prasad, B. L. V. Synthesis of Ag−Pt Alloy Nanoparticles in Aqueous Bovine Serum Albumin Foam and Their Cytocompatibility against Human Gingival Fibroblasts. *Colloids Surf., B* **2009**, 69 (2), 239−245.

(14) Singh, A. V.; Maheshwari, S.; Giovanni, D.; Naikmasur, V. G.; Rai, A.; Aditi, A.; Gade, W.; Vyas, V.; Gemmati, D.; Zeri, G. Nanoengineering Approaches to Design Advanced Dental Materials for Clinical Applications. *J. Bionanosci.* **2010**, 4 (1−2), 1−2.

(15) Singh, A.; Ferri, M.; Tamplenizza, M.; Borghi, F.; Divitini, G.; Ducati, C.; Lenardi, C.; Piazzoni, C.; Merlini, M.; Podestà, A. Bottom-up Engineering of the Surface Roughness of Nanostructured Cubic Zirconia to Control Cell Adhesion. *Nanotechnology* **2012**, 23 (47), 475101.

(16) Singh, A. V.; Rahman, A.; Sudhir Kumar, N.; Aditi, A.; Galluzzi, M.; Bovio, S.; Barozzi, S.; Montani, E.; Parazzoli, D. Bio-Inspired Approaches to Design Smart Fabrics. *Mater. Des.* **2012**, 36, 829−839.

(17) Mak, W. C.; Georgieva, R.; Renneberg, R.; Bäumler, H. Protein Particles Formed by Protein Activation and Spontaneous Self-Assembly. *Adv. Funct. Mater.* **2010**, 20 (23), 4139−4144.

(18) Xie, J.; Lee, J. Y.; Wang, D. I. C. Synthesis of Single-Crystalline Gold Nanoplates in Aqueous Solutions through Biomineralization by Serum Albumin Protein. *J. Phys. Chem. C* **2007**, 111 (28), 10226−10232.

(19) Au, L.; Lim, B.; Colletti, P.; Jun, Y.-S.; Xia, Y. Synthesis of Gold Microplates Using Bovine Serum Albumin as a Reductant and a Stabilizer. *Chemistry—Asian J.* **2010**, 5 (1), 123−129.

(20) Kesarwani, P.; Tekade, R. K.; Jain, N. Spectrophotometric Estimation of Paclitaxel. *Int. J. Adv. Pharm. Sci.* **2011**, 2, 29−32.

(21) Singh, A. V.; Vyas, V.; Maontani, E.; Cartelli, D.; Parazzoli, D.; Oldani, A.; Zeri, G.; Orioli, E.; Gemmati, D.; Zamboni, P. Investigation of in Vitro Cytotoxicity of the Redox State of Ionic Iron in Neuroblastoma Cells. *J. Neurosci.* **2012**, 3 (3), 301−310.

(22) Singh, A. V.; Galluzzi, M.; Borghi, F.; Indrieri, M.; Vyas, V.; Podestà, A.; Gade, W. N. Interaction of Bacterial Cells with Cluster-Assembled Nanostructured Titania Surfaces: An Atomic Force Microscopy Study. *J. Nanosci. Nanotechnol.* **2013**, 13 (1), 77−85.

(23) MacGillivray, R. T. A.; Chung, D. W.; Davie, E. W. Biosynthesis of Bovine Plasma Proteins in a Cell-free System. *Eur. J. Biochem.* **1979**, 98 (2), 477−485.

(24) Xiong, Y.; Washio, I.; Chen, J.; Cai, H.; Li, Z.-Y.; Xia, Y. Poly(vinyl pyrrolidone): A Dual Functional Reductant and Stabilizer for the Facile Synthesis of Noble Metal Nanoplates in Aqueous Solutions. *Langmuir* **2006**, 22 (20), 8563−8570.

(25) Falcaro, P.; Hill, A. J.; Nairn, K. M.; Jasieniak, J.; Mardel, J. I.; Bastow, T. J.; Mayo, S. C.; Gimona, M.; Gomez, D.; Whitfield, H. J. A New Method to Position and Functionalize Metal-Organic Framework Crystals. *Nat. Commun.* **2011**, 2, 237.

(26) Alivisatos, A. P. Naturally Aligned Nanocrystals. *Science* **2000**, 289 (5480), 736−737.

(27) Kim, F.; Connor, S.; Song, H.; Kuykendall, T.; Yang, P. Platonic Gold Nanocrystals. *Angew. Chem., Int. Ed.* **2004**, 43 (28), 3673−3677.

(28) Banfield, J. F.; Welch, S. A.; Zhang, H.; Ebert, T. T.; Penn, R. L. Aggregation-based Crystal Growth and Microstructure Development in Natural Iron Oxyhydroxide Biomineralization Products. *Science* **2000**, 289 (5480), 751−754.

(29) Shankar, S. S.; Rai, A.; Ankamwar, B.; Singh, A.; Ahmad, A.; Sastry, M. Biological Synthesis of Triangular Gold Nanoprisms. *Nat. Mater.* **2004**, 3 (7), 482−488.

(30) Lim, B.; Camargo, P. H. C.; Xia, Y. Mechanistic Study of the Synthesis of Au Nanotadpoles, Nanokites, and Microplates by Reducing Aqueous HAuCl4 with Poly(vinyl pyrrolidone). *Langmuir* **2008**, 24 (18), 10437−10442.

(31) Jin, R.; Cao, Y.; Mirkin, C. A.; Kelly, K. L.; Schatz, G. C.; Zheng, J. G. Photoinduced Conversion of Silver Nanospheres to Nanoprisms. *Science* **2001**, 294 (5548), 1901−1903.

(32) Zeng, J.; Zheng, Y.; Rycenga, M.; Tao, J.; Li, Z.-Y.; Zhang, Q.; Zhu, Y.; Xia, Y. Controlling the Shapes of Silver Nanocrystals with Different Capping Agents. *J. Am. Chem. Soc.* **2010**, 132 (25), 8552−8553.

(33) Marschner, T.; Stief, C. Characterization of 193-nm resist layers by CD-SEM sidewall imaging. *Proc. SPIE* **2003**, 892, 892−900.

(34) Chen, G.; Li, M.; Li, F.; Sun, S.; Xia, D. Protein-Mediated Synthesis of Nanostructured Titania with Different Polymorphs at Room Temperature. *Adv. Mater.* **2010**, 22 (11), 1258−1262.

(35) Henson, P. M. Interaction of Cells with Immune Complexes: Adherence, Release of Constituents, And Tissue Injury. *J. Exp. Med.* **1972**, 134 (3 Pt 2), 114s−135s.

(36) Hennink, W. E.; Champion, J. A.; Katare, Y. K.; Mitragotri, S. Particle Shape: A New Design Parameter for Micro- And Nanoscale Drug Delivery Carriers. *J. Controlled Release* **2007**, 121 (1), 3−9.

(37) Champion, J. A.; Mitragotri, S. Role of Target Geometry in Phagocytosis. *Proc. Natl. Acad. Sci. U. S. A.* **2006**, 103 (13), 4930−4934.

(38) May, R. C.; Machesky, L. M. Phagocytosis and the Actin Cytoskeleton. *J. Cell Sci.* **2001**, 114 (6), 1061−1077.

(39) Iversen, T.-G.; Skotland, T.; Sandvig, K. Endocytosis and Intracellular Transport of Nanoparticles: Present Knowledge and Need for Future Studies. *Nano Today* **2011**, 6 (2), 176−185.

(40) Chithrani, B. D.; Ghazani, A. A.; Chan, W. C. W. Determining the Size and Shape Dependence of Gold Nanoparticle Uptake into Mammalian Cells. *Nano Lett.* **2006**, 6 (4), 662−668.

(41) Chithrani, B. D.; Chan, W. C. W. Elucidating the Mechanism of Cellular Uptake and Removal of Protein-Coated Gold Nanoparticles of Different Sizes and Shapes. *Nano Lett.* **2007**, 7 (6), 1542−1550.

(42) Marsh, M.; McMahon, H. T. The Structural Era of Endocytosis. *Science* **1999**, 285 (5425), 215−220.

(43) Griffiths, G.; Hoflack, B.; Simons, K.; Mellman, I.; Kornfeld, S. The Mannose 6-Phosphate Receptor and the Biogenesis of Lysosomes. *Cell* **1988**, 52 (3), 329−341.

(44) Desai, N.; Trieu, V.; Yao, Z.; Louie, L.; Ci, S.; Yang, A.; Tao, C.; De, T.; Beals, B.; Dykes, D.; Noker, P.; Yao, R.; Labao, E.; Hawkins, M.; Soon-Shiong, P. Increased Antitumor Activity, Intratumor Paclitaxel Concentrations, And Endothelial Cell Transport of Cremophor-free, Albumin-bound Paclitaxel, ABI-007, Compared

with Cremophor-based Paclitaxel. *Clin. Cancer Res.* **2006**, *12* (4), 1317−1324.

(45) Surapaneni, M. S.; Das, S. K.; Das, N. G. Designing Paclitaxel Drug Delivery Systems Aimed at Improved Patient Outcomes: Current Status and Challenges. *ISRN Pharmacol.* **2012**, *2012*, No. 10.5402/2012/623139.

(46) Wei, W.; Ma, G.-H.; Hu, G.; Yu, D.; Mcleish, T.; Su, Z.-G.; Shen, Z.-Y. Preparation of Hierarchical Hollow CaCO$_3$ Particles and the Application as Anticancer Drug Carrier. *J. Am. Chem. Soc.* **2008**, *130* (47), 15808−15810.

(47) Paula, A. J.; Araujo Júnior, R. T.; Martinez, D. S. T.; Paredes-Gamero, E. J.; Nader, H. B.; Durán, N.; Justo, G. Z.; Alves, O. L. Influence of Protein Corona on the Transport of Molecules into Cells by Mesoporous Silica Nanoparticles. *ACS Appl. Mater. Interfaces* **2013**, *5* (17), 8387−8393.

(48) Cifuentes-Rius, A.; de Puig, H.; Kah, J. C. Y.; Borros, S.; Hamad-Schifferli, K. Optimizing the Properties of the Protein Corona Surrounding Nanoparticles for Tuning Payload Release. *ACS Nano* **2013**, *7* (11), 10066−10074.

(49) Danowski, B. Fibroblast Contractility and Actin Organization Are Stimulated by Microtubule Inhibitors. *J. Cell Sci.* **1989**, *93* (2), 255−266.

(50) Merkel, T. J.; Jones, S. W.; Herlihy, K. P.; Kersey, F. R.; Shields, A. R.; Napier, M.; Luft, J. C.; Wu, H.; Zamboni, W. C.; Wang, A. Z. Using Mechanobiological Mimicry of Red Blood Cells to Extend Circulation Times of Hydrogel Microparticles. *Proc. Natl. Acad. Sci. U. S. A.* **2011**, *108* (2), 586−591.

(51) Trebbin, M.; Steinhauser, D.; Perlich, J.; Buffet, A.; Roth, S. V.; Zimmermann, W.; Thiele, J.; Förster, S. Anisotropic Particles Align Perpendicular to the Flow Direction in Narrow Microchannels. *Proc. Natl. Acad. Sci. U. S. A.* **2013**, *110* (17), 6706−6711.